

XMM-Newton EPIC MOS Quiescent Particle Background

K.D. Kuntz^{1*} and S. L. Snowden²

¹ The Henry A. Rowland Department of Physics and Astronomy, Johns Hopkins University, 3701 San Martin Drive, Baltimore, MD, 21218; kkuntz1@jhu.edu

² Code 662, NASA/GSFC, Greenbelt, MD, 20771; Steven.L.Snowden@nasa.gov

Received XX Month 2XXX / Accepted XX Month 2XXX

ABSTRACT

Context. *XMM-Newton* observations of diffuse X-ray emission that fills the field of view require carefully constructed instrumental background spectra for analysis. A method of constructing such backgrounds was proposed in Kuntz & Snowden (2008) but more recent work suggests that that method is insufficient.

Aims. We revisit the analysis of the *XMM-Newton* European Photon Imaging Camera (EPIC) MOS quiescent particle background (QPB) using a factor of XXX more data than were available for our previous analysis in order to determine whether the QPB spectrum is time variable as well as to characterize the “anomalous” states.

Methods. We use the “corner data” to characterize the QPB spectral shape as a function of epoch, spacecraft location, QPB rate, and the deviation of the QPB rate from a ten orbit running mean.

Results. We find that our new characterization of the anomalous states reduces the variation in the QPB spectral shape. However, there remains significant variation in the shape of the QPB spectrum that is primarily due to the spacecraft location. The bulk of the data (?) in the archive was obtained in a region where there is little variation in the spectral shape. There is some slight evidence for variation of the shape of the QPB spectrum with epoch.

Conclusions. While the previously proposed method of background construction is adequate, it can be substantially improved using the expanded archive of corner data. Use of a mean background spectrum will require more careful temporal filtering of the data to remove the time periods when the spacecraft is in regions with a different QPB spectrum shape. Conversely, the current corner data archive can be used to construct QPB spectra to match the expected variation over the course of the observation.

Key words. Instrumentation: miscellaneous – X-rays: diffuse background

1. Introduction and Motivation

Given its large grasp, *XMM-Newton* is the premier instrument with which to study soft extended X-ray emission, particularly on large scales. *XMM-Newton* is especially powerful for surveying large areas (multiple square degrees) for the study of diffuse Galactic emission, the Galactic halo, the Magellanic Clouds, and other nearby galaxies. Such studies require the careful characterization of the non-cosmic backgrounds since the emission of interest can fill the entire field of view (FOV) which precludes the use of local background subtraction methods. These concerns motivated our first study of the *XMM-Newton* background, Kuntz & Snowden (2008, henceforth KS08), which was focussed primarily on the particle-induced background. That study was restricted to the EPIC MOS instrument. The pn instrument, having a significantly longer read time and consequently larger out-of-time event rate, requires a more complex analysis which will be addressed in a companion work.

The particle-induced background is due to energetic particles striking the detector (the CCDs) and its surroundings. Energetic particles striking the detector directly generally produce signals readily distinguishable from X-rays, that is, their energy is too high or the pattern of triggered CCD pixels is incorrect. Energetic particles striking materials around the detector can produce backgrounds in three ways. First, they can produce Auger electrons that, striking the detector, can produce signals that mimic those of X-ray photons. This signal is expected to be

a continuum. Second, they can produce Bremsstrahlung emission, another smooth continuum. Third, they may produce X-ray fluorescence, a line spectrum. This spectrum is expected to vary across the detector due to the proximity of the emitting material. We refer to the recorded spectrum produced by particles and the fluorescent X-rays as the background spectrum, while the energy distribution of the particles themselves will be referred to as the particle spectrum.

Phenomenologically, there are at least three particle populations that produce the particle background (either directly or indirectly), particles from the radiation belts, the “soft protons” responsible for the “soft proton flares”, and Galactic cosmic rays. KS08 showed that, although there were correlations between spectral shape and the flare strength, the spectrum of the soft proton flares was highly variable. As a result, we suggested that periods affected by soft proton flares be removed from analysis, rather than attempting to model the background during those periods. Similarly, the periods of high background due to the particle belts, occurring when *XMM-Newton* is near apogee are to be removed as that spectrum is expected to be quite variable as well. We refer to the background spectrum of the remaining periods as the quiescent particle background (QPB) spectrum. The QPB spectrum is due to some residual soft protons, some contribution due to the particle belts, and a contribution due to Galactic cosmic rays. This last component is anticorrelated with the solar activity as the magnetic field configuration at solar maximum reduces the density of cosmic rays reaching the inner solar system. Figure 1 shows the QPB rate in the XXX-XXX keV band as a function of revolution (orbit number) as well as the sunspot

* This work supported by the GSFC XMM GOF.

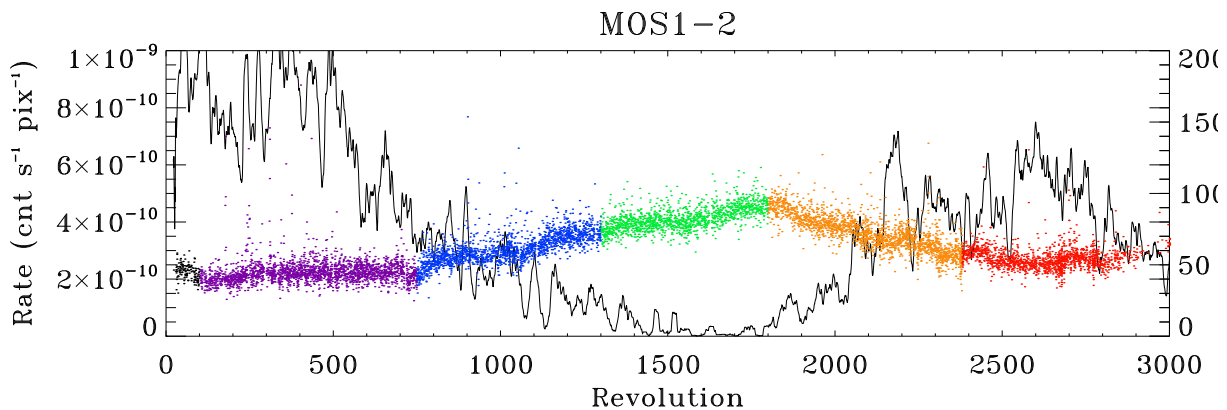


Fig. 1. The QPB rate for MOS1-2 as a function of revolution. The color coding breaks the data into six epochs that will be used later. *Black line:* the sunspot number, showing that the QPB rate is roughly anticorrelated with the solar activity. The color coding marks different epochs, which will be used later in this study.

number; the two are clearly anticorrelated. Note that one can also see the effect of the rather weak solar maximum which we are currently exiting.

The mean QPB spectra for the EPIC MOS instruments are shown in Figure 2. Besides the continuum due to Bremsstrahlung and secondary electrons, and the lines due to X-ray fluorescence, there is one other feature of importance, the upturn of the continuum at low energies. This upturn is due to the incompletely collected events; events for which part the charge cloud overlapped the gate structure and was lost (Prigozhin et al., 1998). For the MOS detectors, this feature appear below ~ 0.4 keV.

The design of both of the EPIC instruments (MOS and pn) allows direct simultaneous measurement of the (particle-induced) background as well as the spectrum in the FOV. The outer corners of the instruments have a mask covering a portion of the detectors. That mask blocks X-rays and is sufficiently thick to block the soft protons that produce the soft proton flares, but the mask does not block the energetic particles responsible for the QPB. For the MOS detectors, the masked region is small; only a quarter to a third of each chip (except for chip 1 which has no masking) is masked and some of that region must be excluded due to light leaks. The corner data, the data from under the mask, for any single observation are insufficient to characterize the QPB spectrum of that observation; the signal to noise is simply too low. However, combining data from multiple observations that have the same characteristics (count rate and spectral hardness) can produce a high signal to noise spectrum.

When the filter wheel is in its “closed” position, the detector is shielded to an extent similar to the shielding due to the mask. The filter-wheel-closed (FWC) data provide a measurement of the QPB spectrum within the FOV, but only for very limited intervals. There is, in fact, much more corner data than there are FWC data. As a result, KS08 developed a method to combine the observation specific corner data information with the FWC data to produce a background spectrum that included both the temporal variation and the spatial variation across the detector.

The KS08 study of the corner data from the EPIC MOS showed that different chips had different responses to the particle background. Further, some chips demonstrated *intermittently* very strong enhancements of the background at energies below ~ 1 keV. When a chip exhibits this behavior, it is said to be in an “anomalous state”. KS08 set empirical criteria for determining whether a chip was in an anomalous state. Besides the anoma-

lous states, KS08 found the shape of the QPB spectrum, as characterized by the XXX-XXX keV/XXX-XXX keV hardness ratio, was temporally variable. This variation would not surprising if that the distribution of particle energies varies with time and location, which would certainly be the case if the background were produced by the mixture of a number of populations of particles. Incidentally, such temporal variation has not been observed by *Chandra* (Bartalucci et al., 2014), a point to which we will return.

KS08 led to the implementation of software¹ for the construction of the non-cosmic backgrounds required for the analysis of extended emission. Initially only for the EPIC MOS, these methods were later extended to the EPIC pn. Given the longer read time of the pn, the “soft-proton flares” are more problematic and significantly restrict the amount of data than can be used. Although this software has been widely and quite successfully used for data analysis (over 100 published papers thus far), there are a number of residual issues which could not be addressed by the limited amount of data available for the initial analysis.

With the additional decade of EPIC observations now available, we are better able to address the following questions: Is the instrumental response to the QPB changing with time? Are there changes to the anomalous states, that is, do the characteristics of the anomalous states change and are more chips developing anomalous states? Why is the *XMM-Newton* QPB temporally variable while the *Chandra* QPB is not? Over time we found a number of observations for which the QPB background removal was not as good as we would have expected. Some of these cases could be attributed to solar-wind charge-exchange or a poorly characterized soft-proton flare background. However, there were cases where the MOS spectra did not agree with with the pn spectra. Although there is some possibility that the differences between the MOS and the pn could be due to a difference in their relative responses to the soft proton flares, the shape of the residuals suggested a problem with the QPB spectrum.

Finally, we should note that the original ESAS software was written in an era when most users were content with subtracting a background before fitting their source spectrum. Since then there has been more interest in the simultaneous fitting of both source and background and the use of statistical methods that do

¹ The *XMM-Newton* Extended Source Analysis Software (ESAS), the latest version of which can be found at https://heasarc.gsfc.nasa.gov/docs/xmm/xmmhp_xmmesas.html.

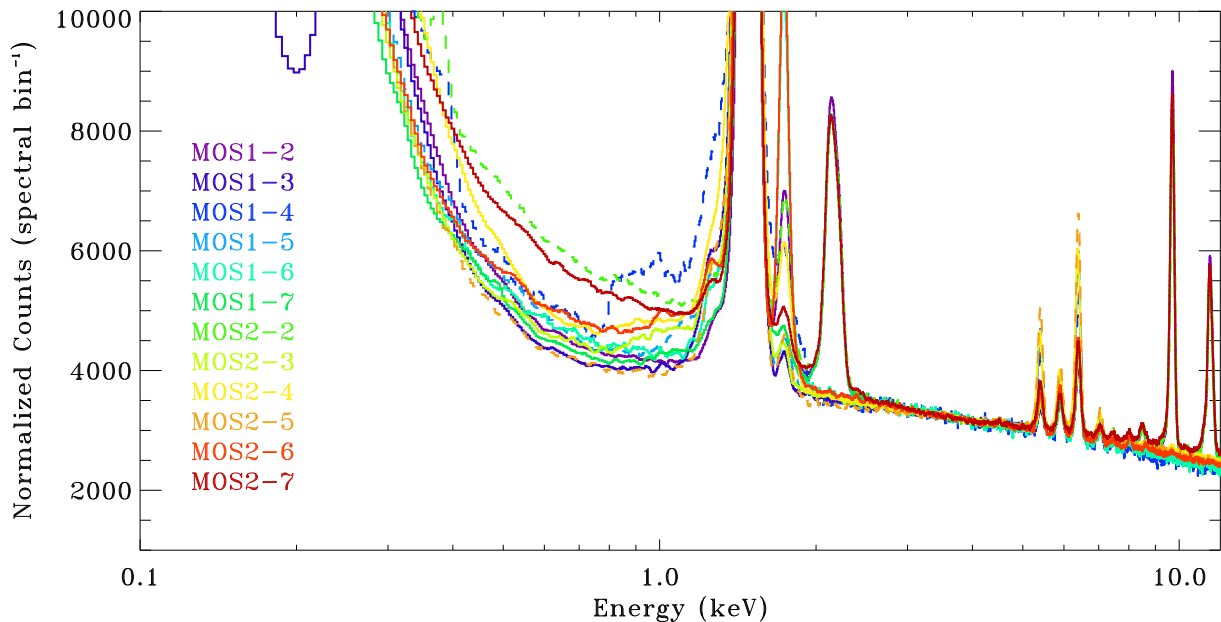


Fig. 2. The mean QPB spectrum for all of the MOS chips. For chips with anomalous states, two spectra are shown, one in the anomalous state, the other with the anomalous periods removed.

not require binning for low count-rate data. Thus there is a need to revise the background construction to support more statistically rigorous methods.

All of these issues suggest that revisiting the QPB would be profitable. Further, with each new software/calibration data release we have modified our methods of deriving the QPB spectrum based on lessons learned from the previous iterations. The method used now is different from that described by KS08. The KS08 study used only the first ~ 5 years of *XMM-Newton* data, comprising ~ 2200 observations and ~ 40 Ms of exposure. For this analysis, we used all data publicly available as of 1 December 2017. We thus have access to $\sim 12,000$ observations and ~ 300 Ms of exposure, before filtering, as is shown in Table ??.

In the following study, we first apply ourselves to determining the QPB spectrum and how its shape varies with time, location, and QPB rate (SS3 & 4). We then consider how one may use this improved understanding to produce better QPB spectra for individual observations (§5). Although we have attempted to avoid discussion of the ESAS implementation of background construction, we hope to provide all the information required should anyone desire to reimplement XMM ESAS, in much the same spirit as the series of *ROSAT* background papers (Snowden et al., 1992; Plucinsky et al., 1993) could allow a new implementation of the *ROSAT* ESAS software.

It should be noted that the quiescent particle background rates in this paper are usually given in $\text{count s}^{-1} \text{ pixel}^{-1}$. These are the standard XMM-Newton software pixels ($0'05$ by $0'05$) not the physical pixels on the devices. Individual chips are denoted by *MOSI-J* where *I* is the detector and *J* is the chip number.

2. Data

The ODF for each observation was downloaded from the HEASARC and run through em-chain in order to apply the most

Table 1. QPB Data Statistics I

Detector	Thin1	Medium	Thick	Closed	Total
Observation Segments					
MOS1	4133	4440	818	102	9500
MOS2	4157	4433	816	98	9509
Exposure Time (Ms)					
MOS1	119.24	130.34	24.82	1.83	276.36
MOS2	120.31	131.17	24.21	1.62	277.37
Counts					
MOS1					
MOS2					

recent calibration (SAS version 16). Ordinarily, one would then filter the event lists to remove periods with soft proton flares. Such was the procedure in KS08. Since then we realized that the mask that forms the FOV is impervious to the soft protons producing the soft proton flares. For observations with strong soft proton flares, the light curves from the region outside the FOV, commonly known as the “corner data”, are flat, as can be seen in Figure ??. Since we are only interested in the data from the “corner data”, there is no need to remove periods with soft proton flares. Removing this filter increases the available data significantly. However, there are still periods of elevated particle background, usually as the spacecraft enters or exits the inner particle belts. We removed these periods using the same algorithm employed to remove the soft proton flares.

We discarded observations where the exposure time after filtering was less than 0.8 of the total exposure. Most of these observations either had peculiar “drop-outs” in the light curve that were mistakenly taken as the base quiescent level. We also discarded observations shorter than 5 ks. **Did we?** We found that 5 ks is too short to distinguish an enhanced QPB rate due to entry into the particle belts from an enhanced (but steady) QPB rate due to other reasons. We also discarded all observations where the filter is “Cal” or the submode is “Unknown”.

We then filtered the event files to exclude events within the FOV as well as all the regions containing scattered light. We extracted the first iteration of QPB spectra on a chip-by-chip basis, and calculated the rate, R count s^{-1} pixel $^{-1}$, in the 0.4-0.8 keV and 2.5-5.0 keV bands as well as the 2.5-5.0 keV/0.4-0.8 keV hardness ratio HR . The total count rate covers the lower energy, higher count rate part of the spectrum, excluding the strong instrumental lines.

For each chip we calculated the long-term light-curve in iterative way. We calculated the mean and root mean square QPB rate for ten orbit bins. For each iteration we discarded observations $> 3\sigma$ from the mean, and recalculated the new mean. We then recalculated the root mean square using all of the data, and repeated. All of the chips had the same light curve shape, but different normalizations. It was not clear whether the normalizations were due to different offsets or to different scalings. We constructed a mean light curve from all of the chips simultaneously and compared it to the light curves from the individual chips. The comparison was slightly closer when assuming that each chip was a scaled version of the mean than by assuming an offset between the chip and the mean. That scaling produces a lower dispersion than the addition of an offset suggests that the bulk of the QPB spectrum is due to the Galactic cosmic rays.

Using the mean light curve, we can determine difference between the QPB rate of a given observation and the rate expected from the mean light curve, or the “normalized rate”:

$$\Delta R \equiv \frac{R - \bar{R}}{\sigma_R} \quad (1)$$

where \bar{R} is the expected rate from the mean light curve and σ_R is the dispersion around the mean light curve.

3. Analysis: Anomalous States

Observations in which some CCDs show an anomalously high low-energy background were noticed early in the *XMM-Newton* mission² Pradas & Kerp (2005) noted these times as the “bright CCD problem”, Stuhlinger (2008) noted them as the “MOS2CCD5 effect” while KS08 referred to them as “anomalous states”. Although the anomalous state can be defined in terms of the behavior of the ratio of the brightest and second brightest pixels within a single event when those two pixels are in the same row, anomalous states are most readily detected through the existence of a low-energy “noise” feature (enhancement) in their spectra and their consequent low hardness ratios. KS08 proposed a set of observational criteria for identifying anomalous states (their Table 1). Further data and consideration suggest that those criteria should be revised.

3.1. Non-Anomalous States

KS08 noted that anomalous states were characterized by low values of HR and high values of R . Since they were not fully aware of the importance of the Galactic cosmic rays in forming the QPB spectrum, they did not know understand the sources of the temporal variation of the rate. Thus, they defined the anomalous states in terms of regions in the R - HR plane. As a result, higher QPB rates due to the long-term light curve could be confused

with higher QPB rates due to anomalous states. For this reason we now use the ΔR - HR plane to define the anomalous states. See Figure 3 for the comparison.

For the chips not showing anomalous data, the mean hardness ratio is roughly four, though there is a significant variation among these non-anomalous chips. Figure 3 (middle) shows the distribution of HR for a chip that does not show anomalous states. Shown in the same plot is the distribution of HR for a simulation of the same set of observations. For each observation, we assume the mean QPB spectrum, calculate the expected number of counts in the 0.4-0.8 keV and 2.5-5.0 keV bands given the measured rate in the 0.3-10 keV band, generate a random Poisson variant for each band, and calculate the resulting hardness ratio. As can be seen, the simulated distribution appears to match the observed distribution, suggesting that the observed distribution is due mostly to statistical variation. If the observed distribution is due to statistical variation, then the mean background spectrum is appropriate for all observations. However, Kolmogorov-Smirnov tests suggest that the two distributions are different, that is, there is a low probability that the measured and simulated distributions could have been drawn from the same population. Thus, there is some temporal variation in the shape of the QPB spectrum.

The right-hand panel of Figure 3 displays the mean spectrum as a function of hardness ratio for a single chip not subject to anomalous states. For this chip, the observations were sorted by the value of HR . The ordered set of observations was then split into ten bins with roughly equal exposure time in each bin, and the mean spectrum was calculated for each bin. Figure 3 plots the ten spectra from lowest value of HR (purple) to highest value (red), where the highest value of HR in each bin is shown to the right of the panel.

For MOS1-2, a chip with no anomalous states, all the spectra are nearly identical. The lowest(highest) two spectra show an increment(decrement) between 0.4 and 0.8 keV, which is due to the way the spectra were sorted. These spectra are from the tails of the distribution, and are typically from the shortest exposures; by sorting based on HR one chooses spectra biased towards positive(negative) noise in the 0.4 to 0.8 keV band, while the other channels, being independent, are unbiased. If, for example, one sorts based on the hardness ratio (2.5-5.0 keV)/(0.2-0.6), the increment/decrement does indeed move to the 0.2 to 0.6 keV band. The bulk of the chips show this same behavior.

3.2. Anomalous States

Figure 4 shows the ΔR - HR plane for the four chips that show anomalous states. It is now clear that the anomalous states can be defined solely in terms of the hardness ratio HR , although what value of HR should be chosen is not always clear.

For the chips with strong anomalous states, the 0.4-0.8 keV decrement can be seen for spectra with high values of HR (See Figure 5.). At the lowest values of HR we do not see the 0.4-0.8 keV increment. Instead, we see an increase at energies below 1 keV. MOS1-4 and MOS2-5 show similar behavior, with a strong jagged profile on a plateau below 1 keV. Since each plotted spectrum is statistically independent of the others, the similarity of the structure among the spectra for a given chip suggests that the structure is real, and not simply due to noise. MOS1-5 and MOS2-2 show a more continuous increase to lower energies. The low energy features in MOS1-5 and MOS2-2 have smaller amplitudes than the structures seen in MOS1-4 and MOS2-5. Further, the low energy features in MOS1-5 and MOS2-2 affect a smaller fraction of observations.

² The first public discussion would appear to be Stuhlinger’s presentation to the *XMM-Newton* CalOps meeting in February 2005. The CalOps meeting presentations can be found at www.cosmos.esa.int/web/xmm-newton/epic-calibration-meetings.

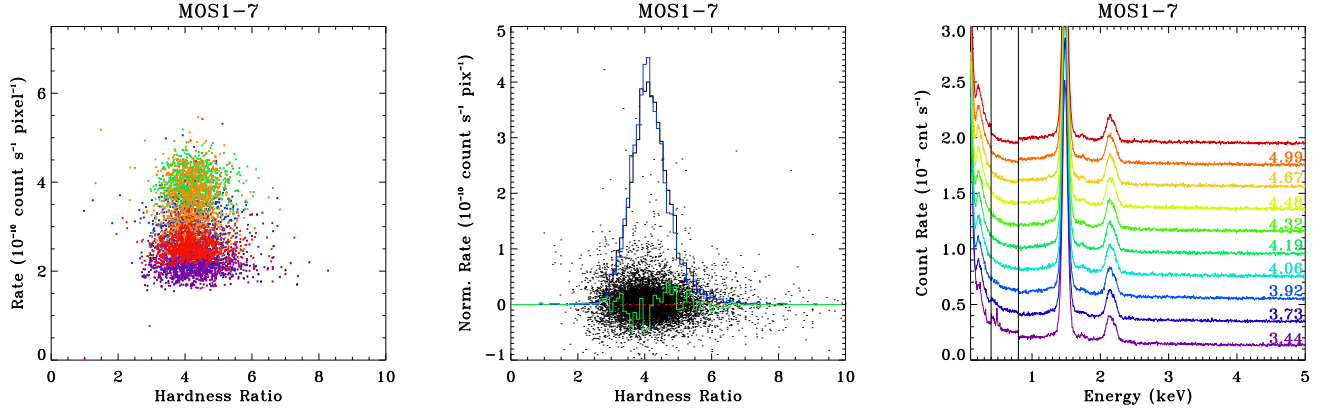


Fig. 3. *Left:* The R - HR diagram for MOS1-2. The points are color coded by the epoch in which they were recorded as in Figure 1. *Middle:* The ΔR - HR diagram for MOS1-2. The points have not been color coded here. The **black** histogram is the distribution in HR while the **blue** histogram is the distribution of HR for a simulated set of observations assuming that the QPB spectrum is temporally invariant. The **red** histogram is the difference between the measured and simulated distributions. *Right:* The mean spectrum as a function of the HR for MOS1-2. The numbers to the far right are the maximum value of HR contained in each spectrum. Each spectrum is offset upwards from the previous spectrum by 2×10^{-5} count s^{-1} . The increment/decrement between 0.4 and 0.8 keV is due to the way the spectra were selected.

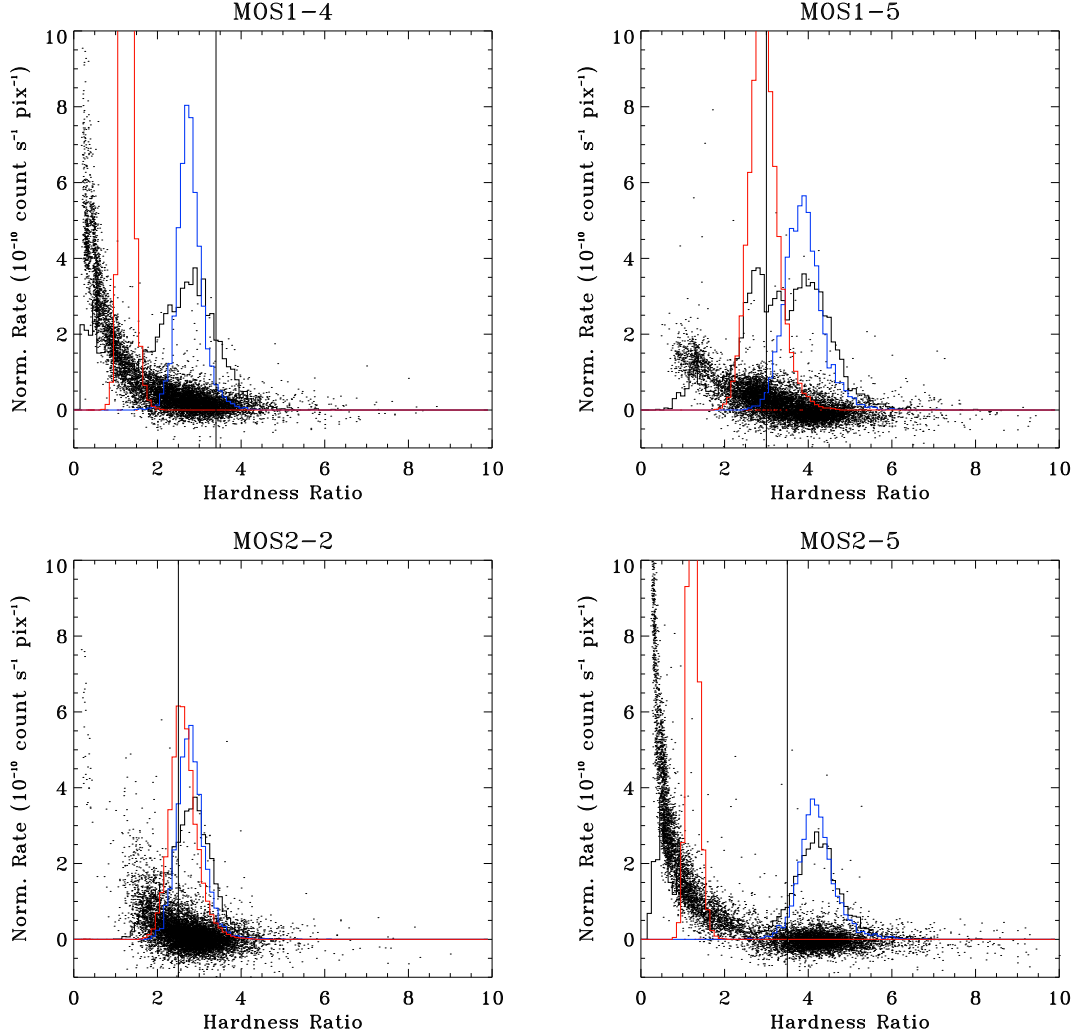


Fig. 4. The differential rate as a function of the (2.5-5.0 keV) to (0.4-0.8 keV) hardness ratio (HR) for the four chips with anomalous states. **Black histogram:** the relative distribution of the values of HR . **Red histogram:** simulated distribution assuming the mean QPB spectrum of that chip and a Poisson distribution for the counts in each spectrum bin. **Blue histogram:** simulated distribution assuming the mean non-anomalous state QPB spectrum of that chip and a Poisson distribution for the counts in each spectrum bin. The solid vertical line shows the approximate upper limit in HR for spectra showing anomalous states which was the limit of the spectra used for calculating the blue histogram.

From the plots of the spectra, one can determine, roughly, the range of HR values that are affected by the low energy feature; $HR \lesssim 3$ for MOS1-5, $HR \lesssim 2.5$ for MOS2-2, and $HR \lesssim 4$ for MOS2-5. It is not clear whether there are unaffected spectra for MOS1-4. The distributions of HR shown in Figure 4 suggests that for chips experiencing anomalous states, there are two overlapping distributions of HR , one due to normal states (similar to that seen for chips without any anomalous states) and one due to the anomalous states. However, there is no clear division in the distributions between anomalous and normal states. Further, the minimum between peaks in the distribution does not correspond at all with the range of anomalous HR suggested by the spectrum plots.

From Figures 4 and 5 it is not clear whether the mean spectra with HR values intermediate between clearly anomalous and clearly normal values are due to a mixture of observations in anomalous states with observations in normal states (where each observation is in one or the other discrete state) or whether there is a variation in the strength of the low energy feature. This ambiguity is resolved if we consider another hardness ratio designed to highlight the high energy edge of the low energy feature. For MOS2-5 we chose the $(0.8-1.0 \text{ keV})/(1.1-1.3 \text{ keV})$ hardness ratio (HR_2); high values indicate a strong low energy feature. Figure 6 shows the distribution in HR_2 for each of the mean spectra plotted for MOS2-5 in the lower-right panel of Figure 5. For this figure we consider only observations with exposures greater than 20 ks in order to ensure that the HR_2 value is not strongly affected by noise. We find that, for a given interval in HR , the HR_2 has a range of values and is clearly not bimodal. This plot suggests that strength of the anomalous state varies with HR , and that any particular slice of HR values does *not* include both normal and anomalous observations. MOS1-4 shows the same behavior. For MOS1-5 and MOS2-2 the hardness ratio $(0.4-0.6 \text{ keV})/(1.1-1.3 \text{ keV})$ shows that the distribution of HR_2 is not bimodal.

For MOS1-4 and MOS2-5, the strength of the low-energy feature increases as HR decreases, as the HR value was designed to show. From the above argument we see that the increase in the strength of the low-energy feature at lower values HR is *not* due to smaller admixture of normal observations at a given HR , but due to a change in the strength of the low-energy feature itself.

At larger values of HR , MOS1-5, MOS2-2, and MOS2-5 do not show the low energy feature. In all three cases there is an extended range of HR values over which the spectral shape does not change significantly. MOS1-4 is more problematic. The spectrum for the decile with $2.44 < HR < 2.73$ shows the same plateau feature seen at lower values of HR . The spectrum of the next higher decile ($2.73 < HR < 2.97$) shows a peak at the same energy as the plateau edge, and that peak persists to higher values of HR . For MOS1-4 there does not appear to be an extended range of high values of HR where the spectrum shape does not change significantly with HR .

A summary of revised anomalous state criteria is given in §5 where we consider

3.3. Other Quasi-Anomalous States

In addition to the anomalous states described above, the same chips showed strong low-energy features before revolution 42. For most of these chips, the low energy feature has a different shape than the low energy feature in the anomalous states after revolution 42. Because there are limited observations before revolution 42, and very limited data with which to characterize the

Table 2. Title

Chip	K-S Probability	Comment
MOS1-2	0.07	
MOS1-3	0.0011	chip lost XXXX-XX-XX
MOS1-4	0.0	Anomalous
MOS1-5	0.0	Anomalous
MOS1-6	0.0006	chip lost XXXX-XX-XX
MOS1-7	0.012	
MOS2-2	0.0	Anomalous
MOS2-3	0.46	
MOS2-4	0.0	
MOS2-5	0.00001	Anomalous
MOS2-6	0.0	
MOS2-7	0.014	

background those periods will be excluded from further consideration.

MOS1-6 also shows unusually low values of HR before revolution 42, and only occasionally thereafter. However there are no clear low energy features in those spectra. Since MOS1-6 was lost to a micrometeorite strike in revolution 961, there are insufficient data to further explore this issue.

4. Analysis: Temporal Variation

As shown in §3.1, chips not showing anomalous states show temporal variability. Taking the mean QPB spectrum for such a chip and using it to simulate the all of the QPB spectra from that chip does not produce the observed distribution of HR , although a visual comparison the measured distribution of HR and distribution of HR derived from the simulated data (Figure 3) would indicate a relatively good match. A two-sample Kolmogorov-Smirnov test comparing the measured values of HR with the simulated values of HR show low probabilities of being drawn from the same sample (Table ??). For each chip the simulations were made for Revolution > 50 , exposure times > 20 ks, and “cleaned” exposure time 0.8 of the total exposure time. These criteria were set to provide the cleanest statistical test of the simulation. In order to allow reproducibility among the multiple analyses, for each chip the entire database of observations was simulated 100 times. For chips showing anomalous states, the observations not in anomalous states were simulated but, given the difficulty of determining the HR boundary for the anomalous states, the import of such simulations is not clear.

The K-S test suggest that mean QPB spectrum is not an adequate description of the QPB spectrum of (at least some) individual observations. Thus we need to determine 1) the amplitude of the difference between the individual QPB spectrum and the mean QPB spectrum, 2) the number of spectra for which the difference is greater than the uncertainty, and 3) the reason for the difference. Given that the difference between the mean spectrum and the individual spectra was noticed only by statistical analysis of the entire database, proceeding from the first question to the third is not feasible. If, however, we can determine the source of the differences, then one can group data appropriately to obtain higher signal-to-noise spectra that will accentuate the differences.

There are a limited number of (known) parameters that might influence the QPB spectrum.

Epoch: It is known that the detectors are evolving/aging, which could change their response to the particle background. However, since the bulk of the QPB is likely to be X-rays produced by particle interaction with the materials surrounding the

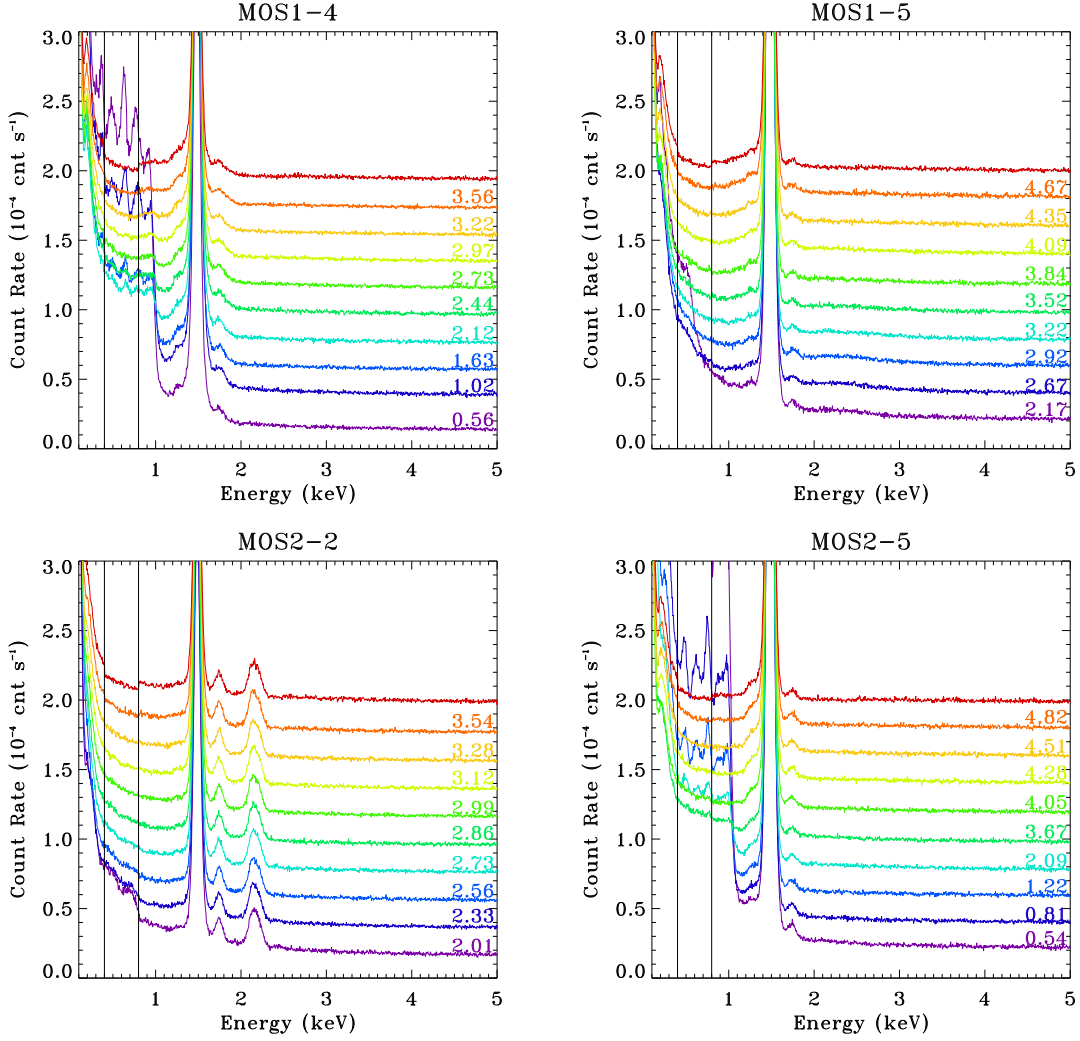


Fig. 5. The mean spectrum as a function of the (2.5-5.0 keV) to (0.4-0.8 keV) hardness ratio (HR) for the four chips with strong anomalous states. The numbers to the far right are the maximum value of HR contained in each spectrum.

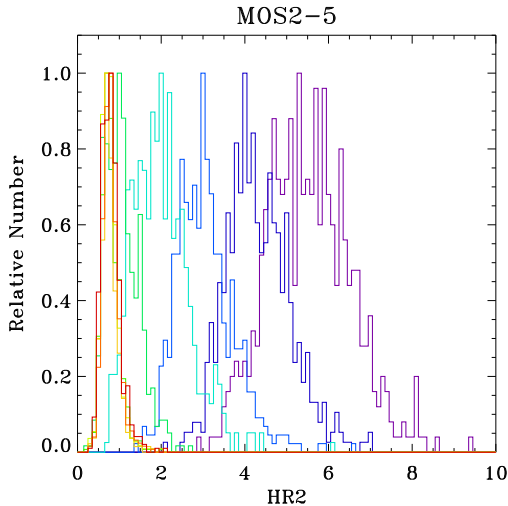


Fig. 6. The distribution of the (0.8-1.0 keV) to (1.1-1.3 keV) hardness ratio (HR_2) for each of the spectra shown for MOS2-5 in the lower right panel of Figure 5. The colors used here match those in the spectrum plots. In this case, only observations with exposures longer than 20 ks were used.

detector, such changes should be tracked by the instrument response.

Rate: Both the strength and spectrum of the Galactic cosmic rays varies with solar cycle (Unknown, 0000). Since the some large fraction of the QPB spectrum is produced by Galactic cosmic rays, even though indirectly, it is not unreasonable that the variation of the QPB spectrum might be due to the variation of the Galactic cosmic ray spectrum. Since the shape of the Galactic cosmic ray spectrum varies with its flux, we can search for spectral variations as a function of the QPB rate.

Normalized Rate: Although the long-term light curve is well correlated with the solar cycle, there is substantial scatter around the mean light curve. Since we know that the near-Earth radiation environment does contribute to the background spectrum (i.e., the instrument is turned off when *XMM-Newton* is too close to the Earth), it is not unreasonable that the scatter around the mean light curve is due to the variation in the contribution of that radiation environment³. Thus the normalized rate may trace the variation due to the spacecraft location.

Location: Since we know that there are spectral changes around perigee (here the unpublished work of Andrea Tiengo

³ Note that at this point I am leaving the definition of “radiation environment” rather open ended, for reasons that will be clear shortly

was particularly informative) it seems particularly useful to start with location. Once we determine how the spectrum varies with location, we can hold the location fixed and determine how the spectrum changes with the other variables.

4.1. Location & Normalized Rate

We will first demonstrate that, on average, ΔR is a function of spacecraft location and tracks the low energy particle populations measured by the *XMM-Newton* Radiation Monitor. However, the dependence of ΔR on location is also dependent on the season (solstice or equinox). We will then demonstrate that QPB spectrum itself depends primarily upon ΔR . The statistics for comparing different locations at the same ΔR are poor, but suggest variation as a function of location.

4.1.1. Location

From the light-curves of individual observations it is known that as the spacecraft approaches perigee the particle background increases. As noted in §2, we have applied the same filtering techniques used to remove the soft proton flares from data within the FOV to filter out high-background times from the corner data. However, those techniques are not entirely successful: a clear increase in the particle background sometimes (often) falls below the 3σ criteria used to remove high-background time periods and sometimes the observation is sufficiently short that it does not contain a true quiescent period with which to compare. As a result, time periods containing enhanced background due to the spacecraft's entry into the particle belts have not been completely excluded from the corner data. Such periods are likely to remain in the user's data as well. There are two issues involved: at what location does the background increase, and does the spectral shape change as a consequence?

Since the soft proton filtering is done with the 2.5-8.5 keV band, we already had light curves in that band for all observations. We created a mean long-term 2.5-8.5 keV band light curve, and created a 2.5-8.5 keV band normalized rate as described by Equation 1. To determine where the background is enhanced, we plotted the normalized rate as a function of spacecraft location, where the normalized rate was summed over the four MOS2 chips without anomalous states. (Since two of the non-anomalous chips of MOS1 are no longer useable, we assume that the MOS2 analysis is applicable to MOS1 as well.) The spacecraft position, $\text{GSM-X}, \sqrt{\text{GSM-Y}^2 + \text{GSM-Z}^2} \equiv P$, was binned in $0.1 R_E \times 0.1 R_E$ bins.

It is well known that the position of the magnetopause (the division between the region containing the terrestrial magnetic field and the region containing the magnetic field flowing with the solar wind) varies with the dynamic pressure of the solar wind. As the magnetopause moves in and out, the region containing the particle belts is similarly compressed and *vice versa*. Thus, rather than considering the background spectrum as a function of the spacecraft's absolute position with respect to the Earth, we consider it as a function of the spacecraft's location with respect to the instantaneous magnetopause.

We use a common formulation for the magnetopause location and shape (Shue et al., 1998):

$$R_0 = (10.22 + 1.29 \tanh(0.184(B_z + 8.14)))P_{dyn}^{(-1/6.6)} \quad (2)$$

$$\alpha = (0.58 - 0.007B_z)(1 + 0.024 * \log(P_{dyn})) \quad (3)$$

$$R = R_0(2./(1. + \cos(\theta)))^\alpha \quad (4)$$

where θ is the angle between the direction of interest and the Earth-Sun line, $P_{dyn} = \mu m_p n_\infty v_\infty^2$ is the dynamical pressure of the solar wind as determined from the solar wind proton density and velocity, and B_z is the component of the interplanetary magnetic field parallel to GSM-Z. It should be noted that as the dynamical pressure increases, the stand-off distance decreases and the shape of the paraboloid changes. For each time step we scale the spacecraft's location with respect to the magnetopause to the same relative position with respect to the magnetopause at a standard P_{dyn} and B_z , 2.5 nPa and 0 nT. That is, for a spacecraft at R we determine the distance to the magnetopause in the direction \hat{R} , for both the instantaneous solar wind conditions, R_c , and the standard solar wind condition, R_s , and scale the spacecraft location to $R_n = RR_s/R_c$. The instantaneous magnetopause distance was determined using the solar wind parameters from the OMNIWeb⁴. This scaling method was previously used in the Walsh et al. (2014) study of the source of the soft proton flares seen by *XMM-Newton*.

The normalized rate as a function of location, shown in Figure 7 is relatively uniform over much of the area sampled by the spacecraft. Noticeable is the higher rate inside the magnetopause on the dayside of the Earth, particularly within $R = 10 R_E$. The region inside the magnetopause, outside of $R = 10 R_E$, and on the nightside of the Earth also appear relatively uniform, though slightly higher than the region outside the magnetopause. Due to the lower signal to noise, it is not clear from this diagram whether the normalized rate decreases outside the bowshock or not. However, see the statistics in Table 3.

The region with an enhanced normalized rate is the region that is also occupied by enhanced energetic particle rates. The lower two panels of Figure 7 show the *XMM-Newton* radiation monitor rates for two bands. The LE1 band measures the flux of electrons with $160 \text{ keV} < E < 1 \text{ MeV}$ and protons with $1 \text{ MeV} < E < 1.5 \text{ MeV}$ while the LE2 band measures the flux of electrons with $1 \text{ MeV} < E < 1.5 \text{ MeV}$ and protons with $1.5 \text{ MeV} < E < 4.5 \text{ MeV}$. With the exception of a few locations dominated by strong transient particle storms (in black), the LE1 band shows a clear structural similarity to the normalized rate map, while the LE2 band shows little correlation with anything. The value of LE1 that tracks the magnetopause closely is $\sim 100 \text{ count s}^{-1}$. It should be kept in mind that the radiation monitor data is not calibrated, and was only intended to warn the spacecraft of high particle fluxes, so that the instruments could be shut down safely. Further, radiation monitor data is missing for quite a few orbits, and there is often significant delay in processing the radiation monitor data⁵, so it cannot be relied on for cleaning the EPIC data.

It should be noted that these particles are not the traditional "trapped particle radiation belts" or "van Allen belts". Those belts contain much higher energy particles ($>40 \text{ MeV}$ protons) that are restricted to radii less than $\sim 2.5 R_E$. A portion of these particles may be due to the ring current, which extends to $9 R_E$ in the equatorial plane (shown by red contours in Figure 8). Due to the Earth's field, the z-extent of the ring current is not expected to be greater than $9 \cos(\theta)^2$, where θ is the angle from the magnetic equator. Figure 8 shows the normalized rate and the LE1 band of the radiation monitor in a different projection. Here we plot $(X^2 + Y^2)X/|X|$ versus Z . This projection rotationally sums over the octants centered on noon (right) and the midnight (left). Again we see that the normalized rate tracks the energetic particle population seen in the LE1 band.

⁴ https://omniweb.gsfc.nasa.gov/ow_min.html

⁵ currently on the order of two years

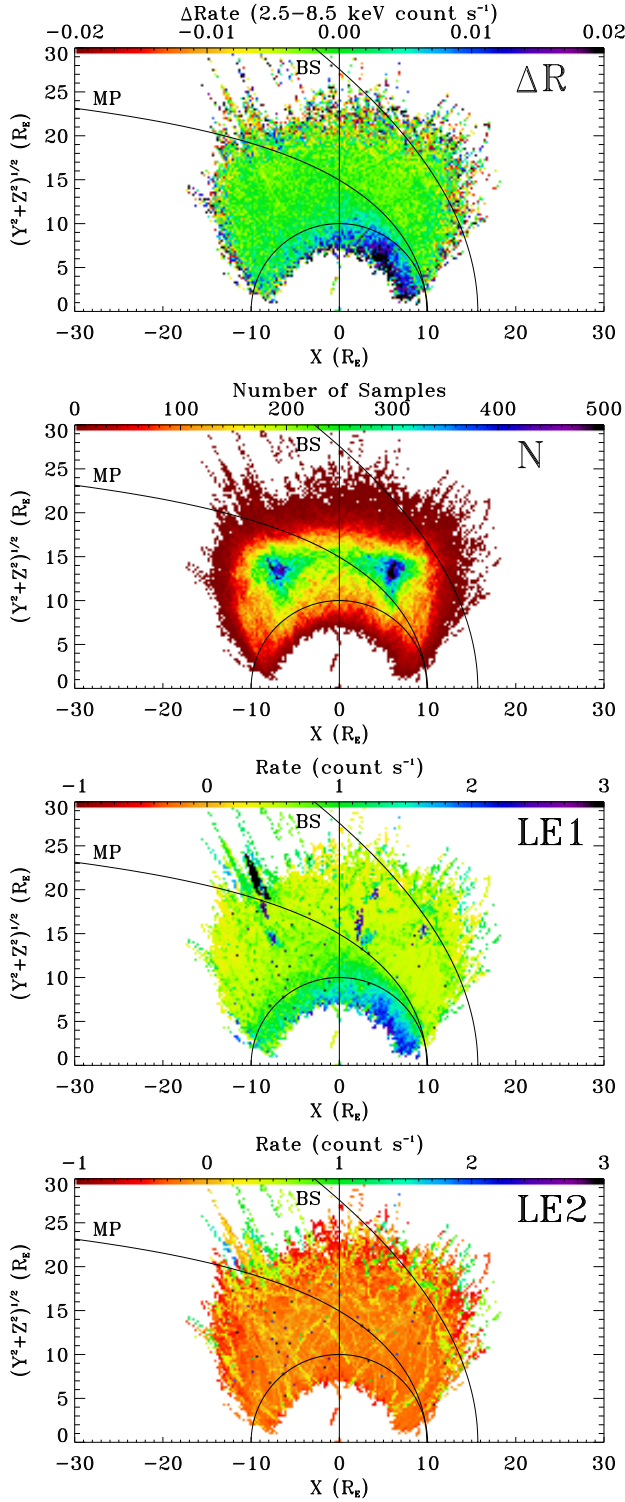


Fig. 7. *Top* (ΔR): The mean normalized rate as a function of spacecraft location in GSM coordinates. The spacecraft position is plotted with respect to the standard magnetopause; the scaling is described in the text. Over plotted are the locations of $R = 10 R_E$, the location of the standard magnetopause (MP), and the location of the standard bowshock (BS). The sun is to the right. *Upper Middle* (N): The number of samples at each location. *Lower Middle* ($LE1$): The radiation monitor LE1 band which measures the flux of electrons with $160 \text{ keV} < E < 1 \text{ MeV}$ and protons with $1 \text{ MeV} < E < 1.5 \text{ MeV}$. The scale is logarithmic. *Bottom* ($LE2$): The radiation monitor LE2 band which measures the flux of electrons with $1 \text{ MeV} < E < 1.5 \text{ MeV}$ and protons with $1.5 \text{ MeV} < E < 4.5 \text{ MeV}$. The scale is logarithmic.

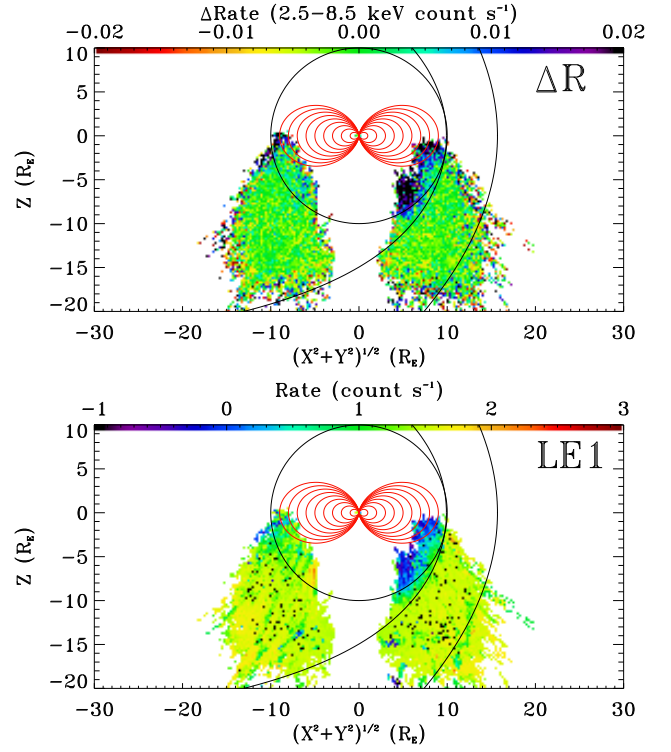


Fig. 8. *Top* (NR): The mean normalized rate as a function of spacecraft location in GSM coordinates. The spacecraft position is plotted with respect to the standard magnetopause; the scaling is described in the text. The data on the right side of the plot are for the octant centered on noon, while the left side of the plot are for the octant centered on midnight. *Bottom* ($LE1$): The radiation monitor LE1 band which measures the flux of electrons with $160 \text{ keV} < E < 1 \text{ MeV}$ and protons with $1 \text{ MeV} < E < 1.5 \text{ MeV}$.

Part of the region of elevated particle flux (day-side near the magnetic equator) corresponds to the region occupied by the ring-current. The same is not seen as strongly on the night-side⁶. The high particle density is seen within the red contour in the dawn and dusk octants as well. Another region of enhanced particle density can be seen on the day-side below the region occupied by the ring current. For this region, the particle density is higher in the noon octant, but still quite visible in the adjacent day-side octants, but not the dawn-dusk octants. This enhancement depends upon the season, being stronger at the June solstice. Since *XMM-Newton* does not sample the same region in the north, we do not know if this distribution is symmetric. It should also be noted that as the *XMM-Newton* orbit precesses the spacecraft samples different regions in different seasons. Thus, any attempt to understand seasonal variation will be complicated by the effects of the solar cycle. Indeed, there is currently almost no data for some combinations of local hour and season.

⁶ The scaling by the solar wind pressure should not have been applied on the night side. One could modify the scaling as a function local hour but this becomes quite complicated. Thus, in this figure, the night-side data points are too close to the Earth. Conversely, the dipole (red contours) should, in reality, be stretched tailward. Whether or not *XMM-Newton* detects (or should detect) the plasma sheet is a question for further work. One further note is that the maps in Figure 8 are averaged over the mission since revolution 50, so they represent the mean behavior. There is seasonal variation as well, leading to higher ΔR and particle densities on the night-side mid-plane during the December solstice.

Table 3. Region Statistics

Region	Description	Number Fraction (Ms)	Exposure	Exposure Fraction	R		ΔR
					10^{-9} count s^{-1} pix $^{-1}$	10^{-9} count s^{-1} pix $^{-1}$	
A	Dayside, $R_n < R_E$	0.22	14.4	0.05	0.44	0.18	
B	Nightside, $R_n < R_E$	0.19	13.9	0.05	0.32	0.05	
C	Dayside, $R_n > R_E$ & $R_n < R_{MP}$	0.08	0.29	23.8	0.30	0.02	
D	Nightside, $R_n > R_E$ & $R_n < R_{MP}$	0.41	0.26	124	0.27	0.007	
E	Magnetosheath ($R_{MP} < R_n < R_{BS}$)	0.41	0.25	125	0.26	-0.0037	
F	Trans-bowshock ($R_n > R_{BS}$)	0.038	0.02	0.21	0.22	-0.0088	

4.1.2. Normalized Rate

Now that we know which regions show enhanced ΔR , we can accumulate spectra from those regions in order to determine whether and how the QPB spectrum changes with location.

We divided the region sampled by the spacecraft into six sub-regions, A through F, based on the X versus $(Y^2 + Z^2)^{1/2}$ diagrams. There are two regions expected to be affected by particle belts that is, $R < 10 R_E$, divided between the dayside (A) and the nightside (B). There are two sub-magnetopause regions that are outside the traditional particle belts but inside the magnetopause, also divided into dayside (C) and nightside (D). The magnetosheath (E) is the region between the magnetopause and the bowshock. Finally, the trans-bowshock region (F) is located outside the bowshock. The location of the bowshock was set using the formulation of (Bennett et al., 1997).

The continuum rate outside the bowshock is 79.6% of the continuum rate inside the bowshock. However, since the spacecraft samples the space outside the bowshock only when the apogee is near the Earth-Sun line *and* the solar wind is relatively high (i.e., typically during solar maximum), the trans-bowshock spectrum was collected only from periods with low QPB rates. Using the mean long-term light curve, one can calculate that the trans-bowshock spectrum should contain only 81.2% of the counts that are in the magnetosheath spectrum. Thus, the rate in the trans-bowshock regions is consistent with the rate in the magnetosheath. The long-term light curve is not sampled uniformly by several of the other regions. Thus we have included in Table 3 the average QPB rate, R , for periods when the spacecraft was in each region, as well as the average ΔR for those periods. Comparison of the two measures of the relative QPB rate readily show the increase in the QPB rate due to the particle belts.

How significant is this? 50% of observations have some exposure time in regions A, B, or C, and XXX% of observations have > 50% of their time in regions A, B, or C.

Understanding the particle populations contributing to the background when the spacecraft is inside the magnetopause is problematic. First, it should be understood that the solar wind data from which one calculates the location of the magnetopause is uncertain, and does not always represent the solar wind actually impinging on the magnetosheath (see ?, for a review). Thus, which side of the magnetopause the spacecraft is on is subject to some error. Second, this region is outside the main belts, and is expected to have a low density of energetic particles. However, despite not being as well studied as the main belts, it is known that the outer-most parts of the belts are very dynamic and can contain strong transient populations of energetic particles. Finally, linking the particle populations with the spectrum observed by the detector is difficult; one needs to know the distribution of particle species and energies and one needs to model all of the interaction of those particles with the materials surrounding the detectors, the distribution of the resulting

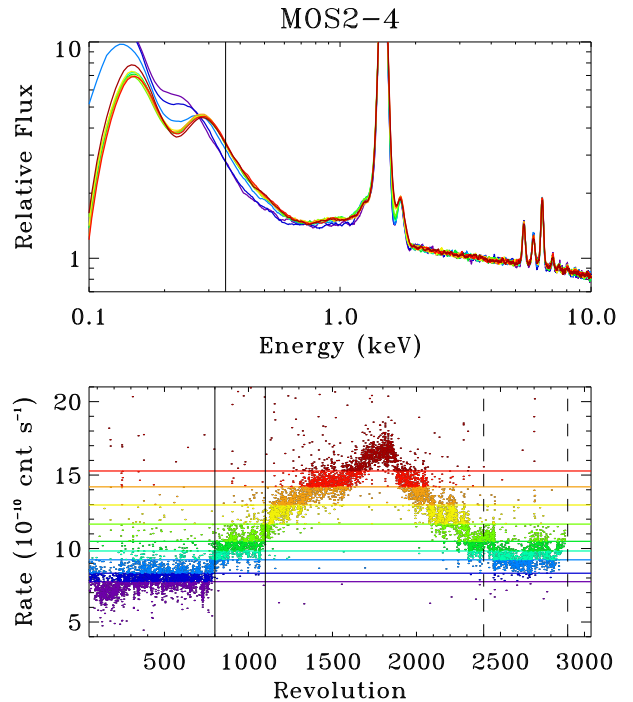


Fig. 9. *Top:* The QPB spectrum as a function of QPB rate for regions D and E. The spectra are smoothed by 55 eV. *Bottom:* The XXX-XXX keV QPB rate as a function of epoch for MOS2-3 using only exposure occurring in regions D and E. The color coding shows a division of the data into 10 rate bins of roughly equal exposure times. The vertical lines indicate the two epochs compared in Figure 10.

electrons produced by those interactions, and the interactions of those electrons with the detector itself. Such modeling is beyond the scope of this work.

4.2. Rate & Epoch

The above analysis showed that location and *mean* ΔR are correlated, and that the spectral shape varies with the location of the spacecraft. However, there are large regions where the variation (as tracked by ΔR) is relatively small. Now we can study just those spectra extracted from one particular region in order to understand how the spectral shape varies with the QPB rate. Given their similarity, we chose time periods in regions D and E to represent the QPB spectrum that is mostly unaffected by the near-Earth radiation environment. However, since the rate is a function of the epoch, disentangling the effects of rate from epoch is not entirely trivial.

Figure 9 displays the QPB spectra as a function of QPB rate as extracted from regions D and E for a single representative

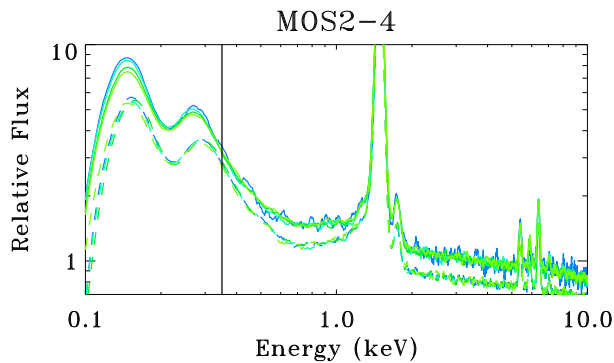


Fig. 10. The QPB spectra from revolutions 800 to 1100 (solid) and revolutions 2400 to 2900 (dashed). The spectra are color-coded using the same scheme as used in the previous figure. The later epoch spectra were shifted down by a factor of 0.8 for clarity. The vertical line is the low energy cut-off placed by earlier background studies.

chip. The observations were sorted by QPB rate and ten rate bins were constructed so that each rate bin contains roughly the same amount of exposure time. The rate bins (shown in the lower panel of the same figure) and the spectra are color-coded by rate. We see that the spectra from the two lowest rate bins show the greatest difference, while the spectra from the highest seven bins show much less variation. However, since the two lowest rate bins include almost no data after revolution 800, it is not clear whether the differences are due to rate or epoch.

Figure 10 displays the QPB spectra in different rate bins for a single chip for two different epochs. The color codes are the same as in Figure 9. The epochs were chosen to provide a significant amount of exposure for a range of rates for two epochs that are well separated in time. For spectra derived from the same epoch but different rates, the spectral shape is relatively constant for energies ≥ 0.2 keV, over the limited range of rates that can be compared within a single epoch. However, for spectra with similar rates, comparison of epochs show strong differences below ~ 0.35 keV and in the low-energy wing of the aluminum line. Thus, for the typical band-pass used, epoch would appear to be of greater importance than the QPB rate. We have compared the lowest three rate bins for revolutions 250-500 with revolutions 500-750, and the highest three rate bins for revolutions 1300-1600 with revolutions 1900-2100. To within the uncertainties we did not see significant changes in shape with rate in those comparisons. **Probably should quantify this, but I'm tired and it's hot.** We would probably need to compare the lowest rate bins with the highest rate bins in order to detect a change in shape with rate.

5. Building QPB Spectra

6. Discussion

6.1. Anomalous States:

It is not clear who first recognized that the excess soft background in the MOS was associated with an excess of events with patterns 2 and 4 (see Figure 12 of KS08), that are events for which the photon energy is split between two pixels in the same row. Unpublished work by Hubert Chen⁷ showed that for events with a total energy E_0 , the energy in the brighter pixel, E_1 and the

⁷ Presented at the April 2009 CalOps meeting, available at www.cosmos.esa.int/web/xmm-newton/epic-calibration-meetings

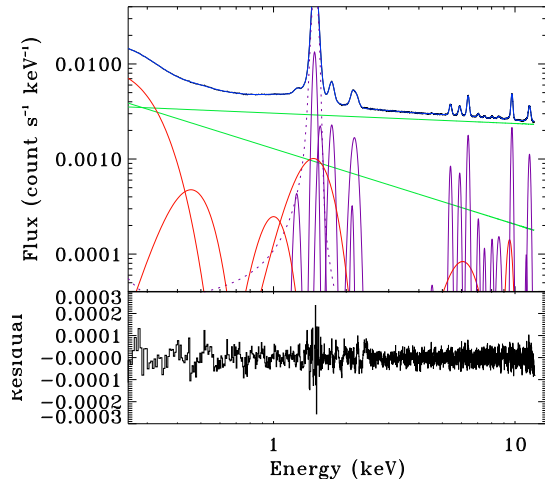


Fig. 11. Fits and residuals to the mean MOS2 spectrum. The spectrum has not been binned or smoothed. We show the complete decomposition of the background spectrum (Black) into its components Green: powerlaw components for the bulk of the continuum, Red: low amplitude features in the continuum fitted with Gaussians, Purple: Gaussian lines, Dashed Purple: Gaussian lines fitted with the instrumental redistribution function. Blue: the sum of the fit components.

energy in the dimmer pixel, E_2 , were correlated with a slope of -0.75 , rather than the expected -1.0 . Chen attributed this behavior to the read-out amplifier circuit rather than a problem with the structure of the CCD itself. Since we have not seen the development of anomalous states in CCDs that did not previously show them, it seems unlikely that anomalous states are due to on-orbit degradation of either the CCDs or the readout circuits.

The transition from an anomalous state to a non-anomalous state has never been observed during a single observation (A. Read, private communication⁸). However, such a statement assumes a bimodal behavior. We have shown that, for observations in any narrow range of the $(2.5-5.0 \text{ keV})/(0.4-0.8 \text{ keV})$ hardness ratio (HR), there is a range strengths of the high energy edge of the low energy spectral feature. Within a narrow band of HR we cannot identify any bimodal behavior that suggests the presence of both anomalous and non-anomalous states. Thus, whatever the root cause of the anomalous states it is, in principal, present in all observations, though it may not be detectable. What we see in the ΔR - HR diagrams are a measure of the strength of its presence.

Thus, it is not unreasonable to attempt to characterize the anomalous state QPB spectra, at least when the low energy feature has a relatively low amplitude, if there is sufficient data.

6.2. Temporal Variation

6.3. IACHEC Best Practices

Traditionally, background spectra have been subtracted from the source spectrum before fitting. The International Astronomical Consortium for High-Energy Calibration (IACHEC) has recommended simultaneous fitting of the source+background spectrum and the background spectrum as such simultaneous fitting allows a more rigorous statistical handling of the data and their uncertainties (Grant et al., 2013, and other IACHEC pub-

⁸ Also presented at the 2010 CalOps meeting, available at www.cosmos.esa.int/web/xmm-newton/epic-calibration-meetings

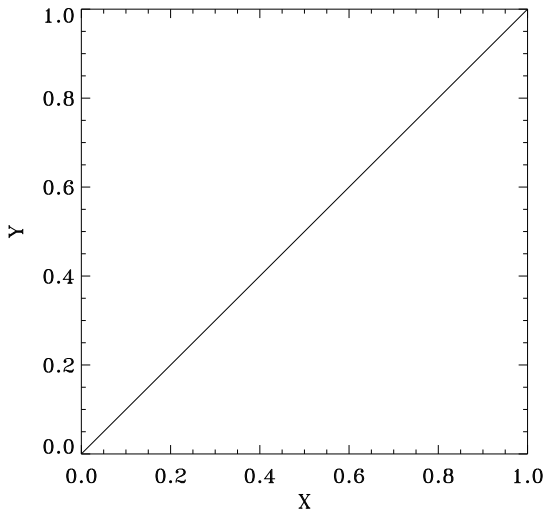


Fig. 12. Caption.

lications). In line with these recommendations we have experimented with fitting the background spectra directly.

We fit the mean background spectra with traditional χ^2 minimization in *xspec* in the 0.25-11.8 keV band for the MOS. The instrumental lines were fit with Gaussians with fitted finite widths. We used the identity matrix for the redistribution because the instrumental redistribution function produced lines that were too broad. That the instrumental redistribution matrix does not work well is not surprising; the mean spectra are composed of many different observations with, potentially, different gains. (Note that the energy uncertainty due to residual gain variations and the charge transfer inefficiency, CTI, correction is ± 5 eV for the MOS⁹.) Although this summation should produce a line that is wider than the instrumental redistribution, the best fit appeared to have been driven by the wings and undersubtracted the line cores. For most of the lines of the MOS, we achieved better fits using the identity matrix for the redistribution. The exception is the Al line which is sufficiently strong that the low energy tail is clearly visible in the data. Most of the lines required a width of $\sigma \sim 0.07$ keV. Most of the lines are clearly identifiable (as per Figure 2) but we did need to introduce a few arbitrary lines to remove residuals, particularly near the Al lines.

The bulk of the continuum requires two power laws and a Gaussian with $E < 0.1$. After the lines were reasonably fit, we found that the continuum had a number of low amplitude humps, some of which are visible to the eye in Figure 11, which could be adequately fit with broad ($\sigma \sim 0.2$ keV) Gaussians. We used a total of 27(24) fit components with a total of 79(70) fit parameters for the MOS(pn) to yield a final χ^2_ν of 1.50(1.45) for 2233(2585) degrees of freedom. The strongest residuals are around the Al lines. Thus, simultaneous fitting of the source and background spectra is a reasonable approach.

7. Summary

This is the summary text

Acknowledgements. We would like to thank Dr. Jean Ballet who recently expressed some misgivings about statistical significance of the variation of the

⁹ EPIC Status of Calibration and Data Analysis, <http://xmm2.esac.esa.int/docs/documents/CAL-TN-0018.pdf>.

Table 4. Title

HJD	E	Method#2	Method#3
1	50	-837	970
2	47	877	230

hardness ratio seen in KS08. It was his suggestion that motivated us to make a complete reprocessing and reanalysis that led to the current work. He was correct, though we would never have been able to demonstrate that with the data available at the time of the original analysis. We also thank Fabio Gastadello for organizing a recent ISSI workshop on the instrumental background. The discussions there with Fabio, Andrea Tiengo, and Simona Ghizzardi led to a number of new directions of inquiry which have resulted in a rather different paper than it would have been otherwise. Presentation of parts of this work at the 2018 IACHEC meeting led to further refinements.

References

- Bartalucci, I., Mazzotta, P., Bourdin, H., & Vikhlinin, A. 2014, *A&A*, 566, A25
 Bennett, L., Kivelson, M. G., Khurana, K. K., Frank, L. A., & Paterson, W. R. 1997, *J. Geophys. Res.*, 102, 26927
 Grant, C. E., Guainazzi, M., Natalucci, L., Nevalainen, J., Plucinsky, P. P., Pollock, A., & Sembay, S. 2013, *ArXiv e-prints*
 Kuntz, K. D., & Snowden, S. L. 2008, *A&A*, 478, 575
 Plucinsky, P. P., Snowden, S. L., Briel, U. G., Hasinger, G., & Pfeffermann, E. 1993, *ApJ*, 418, 519
 Pradas, J., & Kerp, J. 2005, *A&A*, 443, 721
 Prigozhin, G. Y., Rasmussen, A., Bautz, M. W., & Ricker, G. R. 1998, in *Proc. SPIE*, Vol. 3444, X-Ray Optics, Instruments, and Missions, ed. R. B. Hoover & A. B. Walker, 267
 Shue, J.-H., et al. 1998, *J. Geophys. Res.*, 103, 17691
 Snowden, S. L., Plucinsky, P. P., Briel, U., Hasinger, G., & Pfeffermann, E. 1992, *ApJ*, 393, 819
 Stuhlinger, X. X. 2008, Increased low energy noise below 1 keV or the MOS2CCD5 effect., Technical Report XMM-SOC-INST-TN-0033, Issue 1.1, ESA ESOC
 Unknown, A. N. 0000, A Publication, 00
 Walsh, B. M., Kuntz, K. D., Collier, M. R., Sibeck, D. G., Snowden, S. L., & Thomas, N. E. 2014, *Space Weather*, 12, 387

Appendix A: